as described in (*14*), except that 4 mM lactic acid, 2 mM pyruvic acid, and 0.4 mM ascorbic acid were added to the extracellular solution, and 1 mM kynurenic acid was added during the dissection. Pairs of pyramidal neurons and FS cells were recorded in layer V of the visual and somatosensory cortices. Somatic whole-cell recordings were made as previously described in (*14*), except that the intracellular solution contained 0.2 mM EGTA. Data are given as mean ± SEM. Differences were considered statistically significant (Student's t test) if $P < 0.05$. Peaks in the cross-correlogram were considered significant if individual bins exceeded expected values by 2.5 SDs.

26. The latency of the single-axon EPSPs was measured between the peak of the presynaptic action potential and the beginning of the synaptic potential. Average synaptic responses were obtained after aligning the traces by the peak of the presynaptic action potential. Spikes were generated in the pyramidal cells by injecting a brief pulse (3 to 5 ms, 1 nA) of current.
27. Z. F. Mainen, T. J. Sejnowski, *Science* **268**, 1503 (1995).
28. To generate the uncorrelated random currents, a Poisson train (2000 Hz) was convolved with the waveform of a single-axon EPSC, and the result was combined with the convolution of a Poisson train (1000 Hz) and a single-axon IPSC waveform. The waveforms of the synaptic currents were previously recorded (*13*). Trials were separated by 1 to 3 s.
29. PSTHs were built from 200 to 1300 trials. Data were aligned to the peak of the presynaptic spike before constructing the PSTH. To determine the beginning and the end of the PSTH peak, a cumulative sum of the histogram was built after subtracting the baseline spike frequency (*31*). The baseline was defined as a 50-ms period preceding the presynaptic spike.
30. At a holding potential of –70 mV, presynaptic spikes produced unitary EPSCs with an average rise time (10 to 90 %) of 0.43 ± 0.06 ms and a weighted decay time constant of 1.9 ± 0.3 ms [$n = 6$ pairs (Fig. 2A)]. The mean peak amplitude was 185 ± pA (range, 28 to 488 pA; $n = 6$ pairs). The corresponding unitary EPSPs recorded at resting conditions (~ –73 mV) had a rise time of 0.77 ± 0.12 ms and a weighted decay time constant of 9.4 ± 0.9 ms [$n = 7$ pairs (Fig. 2A)]. The mean peak amplitude was 5.3 mV (range, 0.9 to 16.7 mV). The decay time course of unitary EPSCs and EPSPs was fitted with a biexponential function. The weighted decay time constant was calculated as $\tau_w = \tau_1 \times A_1 + \tau_2 \times A_2$, where τ_1 and τ_2, and A_1 and A_2 represent, respectively, the time constant and relative amplitude of each exponential component.
31. T. C. Cope, E. E. Fetz, M. Matsumura, *J. Physiol.* **390**, 161 (1987).
32. C. E. Stafstrom, P. C. Schwindt, J. A. Flatman, W. E. Crill, *J. Neurophysiol.* **52**, 244 (1984).
33. R. Azouz, C. M. Gray, *Proc. Natl. Acad. Sci. U.S.A.* **97**, 8110 (2000).
34. The sim-EPSP with a fast-rising phase was produced by injecting current according to the following equation: $y = A_1[1 - \exp(-t/\tau_{rise1})][\exp(-t/\tau_{decay1})] + A_2[1 - \exp(-t/\tau_{rise2}][\exp(-t/\tau_{decay2}]$, in which y is the amplitude of the injected current, t is time, $A_1 = 150$ pA, $\tau_{rise1} = 0.01$ ms, $\tau_{decay1} = 1$ ms, $A_2 = 70$ pA, $\tau_{rise2} = 3$ ms, and $\tau_{decay2} = 20$ ms. To generate the slow-rising sim-EPSP, current was injected according to the following equation: $y = A[1 - \exp(-t/\tau_{rise})] \times [\exp(-t/\tau_{decay})]$, in which $A = 150$ pA, $\tau_{rise} = 10$ ms, and $\tau_{decay} = 15$ ms.
35. In six pyramidal-to-FS cell connections, both the EPSP and its corresponding EPSC were recorded. A significant correlation between the EPSC decay time constant and the EPSP rise time was observed.
36. Simulated EPSPs with a fast rise time (~0.1 to 0.2 ms, 10 to 90%) and variable decay time courses were generated by injecting current according to the equation $y = A[1 - \exp(-t/\tau_{rise})] \times [\exp(-t/\tau_{decay})]$.
37. C. E. Stafstrom, P. C. Schwindt, M. C. Chubb, W. E. Crill, *J. Neurophysiol.* **53**, 153 (1985).
38. A. M. Thomson, D. Girdlestone, D. C. West, *J. Neurophysiol.* **60**, 1896 (1988).
39. G. Stuart, B. Sakmann, *Neuron* **15**, 1065 (1995).
40. Near-threshold unitary EPSPs were obtained by depolarizing the membrane of the postsynaptic FS cell with square current pulses of 400 ms.
41. The average amplitude of the unitary EPSPs at resting conditions was 0.9 ± 0.1 mV, and at depolarized potentials, it was 1.1 ± 0.2 mV ($n = 5$ pairs, $P = 0.07$).
42. M. Galarreta, S. Hestrin, data not shown.
43. J. R. Geiger *et al.*, *Neuron* **15**, 193 (1995).
44. B. Lambolez, N. Ropert, D. Perrais, J. Rossier, S. Hestrin, *Proc. Natl. Acad. Sci. U.S.A.* **93**, 1797 (1996).
45. M. Martina, I. Vida, P. Jonas, *Science* **287**, 295 (2000).
46. GABA-mediated IPSPs were isolated from the signal mediated via electrical synapses by subtracting the responses obtained at depolarized potentials with those obtained near Cl^- reversal potential.
47. E. H. Buhl *et al.*, *J. Physiol.* **500**, 689 (1997).
48. A. Reyes *et al.*, *Nature Neurosci.* **1**, 279 (1998).
49. M. C. Angulo, J. Rossier, E. Audinat, *J. Neurophysiol.* **82**, 1295 (1999).
50. G. Tamás, E. H. Buhl, P. Somogyi, *J. Physiol.* **500**, 715 (1997).
51. G. Tamás, P. Somogyi, E. H. Buhl, *J. Neurosci.* **18**, 4255 (1998).
52. A. Gupta, Y. Wang, H. Markram, *Science* **287**, 273 (2000).
53. We thank W. T. Newsome for useful comments on the manuscript. Supported by NIH grants EY09120 and EY12114.

6 April 2001; accepted 10 May 2001

Liquid Crystal Alignment on Carbonaceous Surfaces with Orientational Order

J. Stöhr,[1]* M. G. Samant,[1] J. Lüning,[1]* A. C. Callegari,[2] P. Chaudhari,[2] J. P. Doyle,[2] J. A. Lacey,[2] S. A. Lien,[2] S. Purushothaman,[2] J. L. Speidell[2]

We used near-edge x-ray absorption fine structure (NEXAFS) spectroscopy to link the orientational bond order at three carbonaceous surfaces—rubbed polyimide, ion beam–irradiated polyimide, and ion beam–irradiated diamond-like carbon films—with the direction of liquid crystal (LC) alignment on these surfaces. We show that, in general, LC alignment can be created on any carbonaceous substrate by inducing orientational order at its surface. Our results form the scientific basis for LC alignment layers consisting of amorphous carbon films in which orientational order near the surface is induced by a directional low-energy ion beam.

The alignment of a nematic LC, consisting of an assembly of rodlike molecules, on rubbed polymer surfaces underlies the manufacture of today's flat panel displays (*1*). Because of various problems associated with the wet polymer deposition and the mechanical rubbing processes, much research has been devoted to the development of improved methods and materials. So far, this effort has been largely unsuccessful. Although noncontact methods such as ultraviolet (*2–4*) or ion beam (IB) (*5*) irradiation have been suggested, their reliance on polymer substrates has impeded their technological use. A replacement process should be based on an inexpensive substrate material that can be deposited in a dry deposition process on large area panels, required for future applications in desk-top displays. Also, present displays suffer from limited viewing angles, and an improved process should allow the fabrication of microscopic multidomain alignment regions that enable larger viewing angles (*4*). The lack of scientific understanding of the alignment process is another critical factor that has been missing for a device enabling advance.

Early LC alignment models were based on the existence of microgroves at the surface of the alignment film (*6*). Later models invoked epitaxylike effects at the polymer surface where the LC is oriented by a preferred crystalline structure (*7*), microcrystalline nucleation sites (*8*), or crystalline regions with a preferred chain orientation (*9*). The technologically important pretilt angle has been speculated to arise from tilted main or side chain segments at the rubbed polymer surface that "guide" the LC rods (*10*, *11*).

Theoretical advances have been impeded by the complexity of the LC-polymer system, and only specific aspects of the alignment phenomenon have been addressed. The preferred orientation of the LC rods parallel to the surface has been attributed to steric effects between the LC and a flat surface (*12*), and their preferred uni-

[1]IBM Research Division, Almaden Research Center, 650 Harry Road, San Jose, CA 95120, USA. [2]IBM Research Division, T. J. Watson Research Center, Post Office Box 218, Yorktown Heights, NY 10598, USA.

*Present address: Stanford Synchrotron Radiation Laboratory, Post Office Box 20450, Mail Stop 69, Stanford, CA 94309, USA.

axial in-plane alignment has been modeled by a macroscopic theory of van der Waals forces between two semiinfinite anisotropic uniaxial continuous media (*13*). The LC pretilt angle has been explained by the van der Waals interaction between asymmetric LC molecules, hinged to the surface on one side, and the polymer surface, modeled as a continuous semiinfinite dielectric medium (*14*). A general phenomenological theory has explained LC alignment by a molecular interaction that links the orientational order of the LC system to the molecular order at the surface of the alignment substrate (*15*).

We used polarization-dependent near-edge x-ray absorption fine structure (NEXAFS) measurements to determine the nature and order of the chemical bonds at the surfaces of three carbonaceous alignment layers—rubbed polyimide (PI), IB-irradiated PI, and IB-irradiated amorphous carbon films. Our results provide definitive evidence for the molecular nature of the LC alignment mechanism and directly suggest the use of inorganic amorphous carbon films for LC alignment. The scientific understanding of the molecular level alignment process and the convenient dry deposition of thin amorphous carbon layers, which can be made more transparent by addition of hydrogen, form the scientific basis for a device enabling breakthrough. The new LC alignment layers for flat panel displays are based on hydrogenated amorphous, so-called diamondlike carbon (DLC) films with IB-induced orientational order (*16*). The IB process also opens the door for the manufacture of multidomain displays with enlarged viewing angles.

Indium-tin-oxide–coated glass plates were spin-coated with PI to a thickness of less than 100 nm or covered by a thin DLC film (about 10 nm) (*17*), produced by sputtering or chemical vapor deposition with hydrogen content in the 10 to 30% range. Some of the PI samples were rubbed with a rayon-cloth rubbing machine. The other PI samples and the DLC samples were irradiated with a directional beam of neutralized Ar ions with a Kaufman type source at beam energies in the 75- to 300-eV range (*5*). The rubbing direction and in-plane projection of the IB were along the $+x$ axis of our coordinate system, as shown in Fig. 1. The IB incidence angle α from the surface normal was varied in the range 15° to 75°. All LC pretilt angle measurements were carried out with a Merck ZLI-5080 liquid crystal (*5*). For rubbed PIs, the LC director, defined as the average rod direction x, is oriented along the rubbing direction and tilted up by a pretilt angle ε (Fig. 1). For the IB-treated samples, the director is also parallel to x but is tilted up from the $-x$ direction (see Fig. 1).

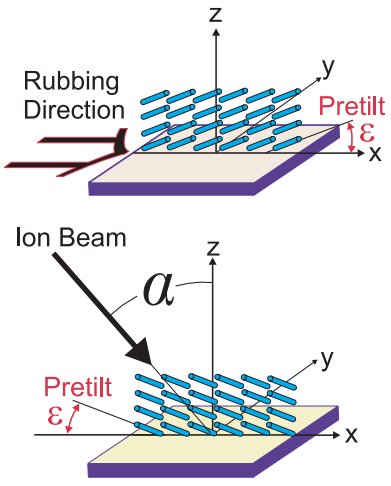

Fig. 1. Experimental geometry and LC orientation on rubbed PI (top) and IB-treated PI and amorphous carbon surfaces (bottom).

NEXAFS measurements were carried out at the Stanford Synchrotron Radiation Laboratory with nearly linearly polarized soft x-rays from the wiggler beam line 10-1, equipped with a spherical grating monochromator. The energy resolution was fixed to about 100 meV at the C K-edge. NEXAFS spectra were recorded by KVV Auger electron (AEY) detection, which samples only the first nanometer below the free surface (*18*). Spectra were recorded in the geometry shown in Fig. 1 with the electric field vector $\vec{E}$ in either the (x, z) or (y, z) plane at an angle θ from the surface normal z. We define θ to be positive for $\vec{E}$ in the $(+x, z)$ and $(+y, z)$ quadrants and negative for $\vec{E}$ in the $(-x, z)$ and $(-y, z)$ quadrants, respectively. The spectra were normalized to the incident photon flux and to the number of C atoms in the sample, as discussed elsewhere (*15*, *18*).

In Fig. 2, we show angle-dependent C K-edge AEY NEXAFS spectra of the rubbed PI and of a PI and DLC film irradiated at $\alpha = 45°$. In the left panel, we compare spectra recorded at normal x-ray incidence with $\vec{E}$ aligned along the x (black line) and y (red line) axes. The right panel shows spectra recorded with $\vec{E}$ oriented in the (x, z) plane at $\theta = 45°$ (black line) and $-45°$ (red line). The three peaks below 290 eV correspond to transitions to π^* orbitals on different C atoms as indicated in the figure, and the peak intensities are quantitatively related to the average number of π^* orbitals per carbon atom and their projection along $\vec{E}$ (*15*). The spectrum of the IB-irradiated PI surface closely resembles that of the IB-irradiated DLC and the DLC film before irradiation (not shown in figure). In particular, the peak at 285 eV, hereafter referred to as peak 1, arises from C=C π bonds in unsaturated, mostly ringlike, structures in an amorphous carbon network (*19*). For the DLC films, the spectral peaks around 286.5 eV and 288.5 eV arise from nitrogen and oxygen contamination. The higher energy σ resonances above 290 eV exhibit the opposite polarization dependence, as expected. For all substrates, the π orbitals have a preferential in-plane alignment along y. In contrast, the out-of-plane orientation in the (x, z) plane is asymmetric with respect to the z axis, favoring the $(-x, z)$ over the $(+x, z)$ quadrant for rubbed PI and vice versa for the IB prepared surfaces. The IB prepared surfaces yielded good LC alignment despite the relatively small asymmetry of the spectra (Fig. 2) (*20*).

The measured intensities of peak 1 for ori-

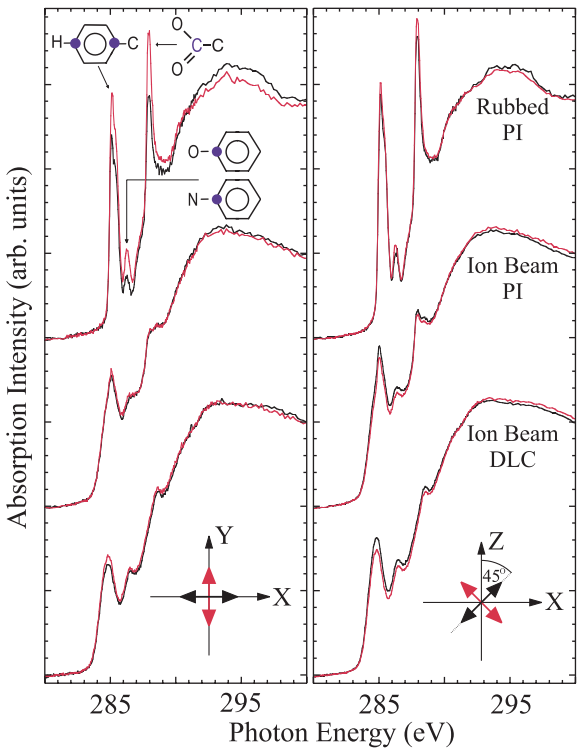

Fig. 2. Polarization-dependent AEY C K-edge NEXAFS spectra for rubbed PI, IB-irradiated PI, and IB-irradiated DLC. Both films were irradiated at an IB incidence angle of $\alpha = 45°$. For the PI film, a beam energy of 75 eV and a dose of 3.8×10^{15} Ar ions/cm^2 were used. The DLC film was irradiated at 200 eV and a dose of 4.5×10^{15} Ar ions/cm^2. The resonances below 290 eV are associated with the π orbitals on different C atoms, indicated as filled circles in the structural formulas. The broad structure near 295 eV corresponds to transitions to σ orbitals. The left column shows the in-plane asymmetry of the spectra and the right column shows the $\pm 45°$ out-of-plane asymmetry. The color of the spectra reflects the orientation of $\vec{E}$ (double arrow) in the respective icons.

entation of $\vec{E}$ in the (x, z) and (y, z) planes are shown in Fig. 3 for the same PI that was either rubbed (Fig. 3B) or irradiated at $\alpha = 45°$ and 100 eV at a dose of 1.5×10^{16} Ar ions/cm^2 (Fig. 3A). The measured intensity of peak 1 in the (x, z) plane, shown as diamonds, is found to be asymmetric with respect to the surface normal. The solid curve through the data points is a fit by the general NEXAFS intensity distribution function (*15*, *21*):

$$I^{xz}(\theta) = a^{\parallel} + b^{\parallel} \cos 2(\theta - \gamma) \qquad (1)$$

where the constants $a^{\parallel}$ and $b^{\parallel}$ are determined by the angular distribution of the π system and the degree of x-ray polarization (*15*) and the angle γ characterizes the average tilt angle of the π bonds at the surface. From the fits, we obtain $\gamma = -6.0° \pm 0.5°$ for the rubbed and $18.8° \pm 1.0°$ for the IB-treated PI. The preferential tilt of the π bonds at the film surface is illustrated in the inset of Fig. 3, A and B. Here we pictured the π orbitals to be perpendicular to the in-plane σ bonds in a ringlike carbon structure. The observed asymmetry is opposite for the rubbed and IB-treated samples.

The intensity asymmetry relative to $\theta = 0$ is absent for the (y, z) plane. The corresponding intensity is shown as open circles in Fig. 3, A and B, fitted by a dashed line according to $I^{yz}(\theta) = a^{\perp} + b^{\perp} \cos 2\theta$. In both cases, our measurements show a larger peak 1 intensity for $\vec{E} \parallel \pm y$ (dashed curve, $\theta = \pm 90°$) than for $\vec{E} \parallel \pm x$ (solid curve, $\theta = \pm 90°$), i.e., a preferential in-plane π bond orientation perpendicular to the rubbing or IB direction.

The opposite sign of γ for the rubbed and IB-treated sample suggests a close link of the bond asymmetry at the film surface with the LC pretilt direction, illustrated in Fig. 1. For IB-treated PI and DLC surfaces, even the magnitude of the LC pretilt angle ε is correlated with γ as shown in Fig. 4. Here we compare the measured LC pretilt angles for samples irradiated at different incidence angles α with the tilt angles measured with NEXAFS. In general, the LC pretilt angle ε depends not only on the substrate orientation alone but also on the chemical composition of the alignment surface and on the LC compound (*14*, *22*). However, in our case, we only change the bond asymmetry through the IB incidence angle so that the used LC (Merck ZLI-5080) only senses the relative change in bond asymmetry. This uniquely demonstrates the direct proportionality between ε and γ.

At the rubbed polymer surface, orientational bond order arises from a preferential alignment of the polymer chains (*15*). For the IB-treated surfaces, orientational order is created by preferential bond breaking and bond formation relative to the incident IB direction. Carbon-carbon bonds and rings oriented perpendicular to the incident IB provide a larger cross section for the IB and are preferentially destroyed over those whose bonds or bonding planes are parallel to the beam direction. Near the irradiated surface, the amorphous carbon network will therefore exhibit a preferential orientation of its σ bonds parallel and π bonds perpendicular to the beam direction, respectively, as observed by NEXAFS.

LC alignment on carbonaceous materials can be understood by consideration of the angle-dependent interaction between two systems, the LC and the alignment surface, using the Landau–De Gennes formalism (*23*). Within this framework, the orientational order of the LC and the alignment surface are described by quadrupole moments of the charge density, and the minimum interaction energy corresponds to an alignment of the eigendirections of the two quadrupoles (*15*). NEXAFS spectroscopy provides a sensitive measure of the quadrupole moment of the molecular π system at the alignment surface. For the alignment surface, the principal axes x', y', and z' of the quadrupole moment form a coordinate system that is rotated by an angle γ about the $y = y'$ axis. The rotation angle originates from the unidirectional surface treatment that destroys the cylindrical molecular symmetry about the surface normal. The left column in Fig. 2 shows that the rubbed polymer surface and the IB-treated surfaces all have the same in-plane quadrupolar charge asymmetry and therefore the in-plane LC alignment direction is along the x axis, in all cases. However, rubbing and IB treatment lead to opposite out-of-plane bond asymmetries, as evident from the right column of Fig. 2. The quadrupolar charge distribution is rotated by γ in opposite directions from the surface normal, as illustrated in Fig. 3. This leads to the two distinctly different pretilt directions illustrated in Fig. 1.

Our results suggest that any method that creates a statistically significant orientational order at the surface of a carbonaceous material can be used for LC alignment. Even materials without translational order, i.e., amorphous materials, may have orientational order because of the strong directional nature of unsaturated carbon bonds (*24*). In general, the anisotropy of carbon bonding increases with unsaturation. Tetrahedral sp^3 bonds are isotropic, sp^2 σ bonds are planar, and sp σ bonds are axial. Hence, disordered systems with π bonding are more readily oriented than those with saturated bonds. Rubbing (*1*), ultraviolet irradiation (*2*–*4*), and IB irradiation (*5*) are examples of methods that can produce orientational order.

In particular, we have shown that amorphous carbon surfaces in which orientational order has been induced by directional irradiation with a low-energy IB can be used for LC alignment. The scientific understanding reported here forms the foundation for flat panel displays that have been manufactured at IBM (*16*).

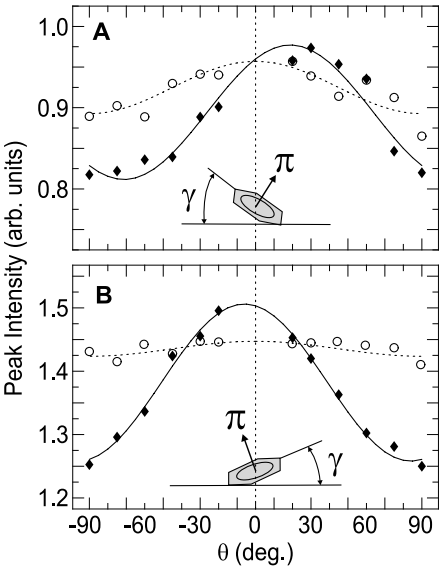

Fig. 3. Peak 1 NEXAFS intensity for IB-irradiated PI (**A**) and rubbed PI (**B**) measured by AEY detection as a function of $\vec{E}$ orientation in the (x, z) plane (diamonds, solid curve) and (y, z) plane (open circles, dashed curve). The insets illustrate the out-of-plane tilts of the π system at the surface, revealed by the data.

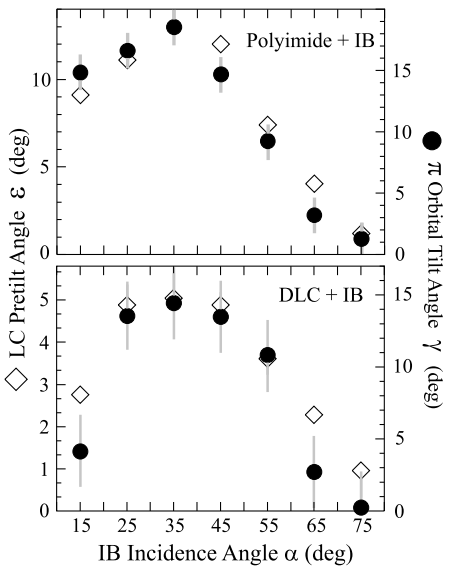

Fig. 4. LC (Merck ZLI-5080) pretilt angle ε and molecular tilt angle γ as a function of IB incidence angle α for PI (PI + IB) (**top**) and DLC (DLC + IB) (**bottom**) films. IB energies and doses of 75 eV and 3.8×10^{15} Ar ions/cm^2 were used for PI and 200 eV and 4.5×10^{15} Ar ions/cm^2 for DLC.

References and Notes

1. S. W. Depp, W. E. Howard, *Sci. Am.* **268**, 90 (March 1993).
2. W. M. Gibbons, P. J. Shannon, S. T. Sun, B. J. Swetlin, *Nature* **351**, 49 (1991).
3. P. J. Shannon, W. M. Gibbons, S. T. Sun, *Nature* **368**, 532 (1994).

4. M. Schadt, H. Seiberle, A. Schuster, *Nature* **381**, 212 (1996).
5. P. Chaudhari, J. Lacey, A. Lien, J. Speidell, *Jpn. J. Appl. Phys. Part 2 Lett.* **37**, L55 (1998).
6. D. W. Berreman, *Phys. Rev. Lett.* **28**, 1683 (1972); *Mol. Cryst. Liq. Cryst.* **23**, 187 (1973).
7. J. M. Geary, J. W. Goodby, A. R. Kmetz, J. S. Patel, *J. Appl. Phys.* **62**, 4100 (1987).
8. H. Mada, T. Sonoda, *Jpn. J. Appl. Phys.* **32**, L1245 (1993).
9. M. F. Toney *et al.*, *Nature* **374**, 709 (1995).
10. K. Y. Han, T. Uchida, in *Proceedings Eurodisplay 1993* (SID, Strasbourg, France, 1993), pp. 13–16.
11. S. Kobayashi, Y. Iimura, *SPIE* **2175**, 122 (1994).
12. K. Okano, *Jpn. J. Appl. Phys.* **22**, L343 (1983).
13. _____, N. Matsuura, S. Kobayashi, *Jpn. J. Appl. Phys.* **21**, L109 (1982).
14. X. Zhuang, D. Wilk, L. Marruci, Y. R. Shen, *Phys. Rev. Lett.* **75**, 2144 (1995).
15. J. Stöhr, M. G. Samant, *J. Electr. Spectrosc. Relat. Phenom.* **98**, 189 (1999).
16. P. Chaudhari *et al.*, *Nature* **411**, 56 (2001).
17. J. Robertson, *Surf. Coatings Technol.* **50**, 185 (1992).
18. M. Samant *et al.*, *Macromolecules* **29**, 8334 (1996).
19. G. Comelli, J. Stöhr, C. J. Robinson, W. Jark, *Phys. Rev. B* **38**, 7511 (1988).
20. Despite the relatively small in-plane asymmetry of the spectra for the IB-irradiated DLC relative to the rubbed PI sample (Fig. 2), the measured in-plane LC anchoring energies for the two samples are about the same.
21. K. Weiss *et al.*, *Macromolecules* **31**, 1930 (1998).
22. K.-W. Lee, S. Paek, A. Lien, C. Durning, H. Fukuro, in *Polymer Surfaces and Interfaces: Characterization, Modification and Application*, K. L. Mittal, K.-W. Lee, Eds. (VSP, The Netherlands, 1996), pp. 295–315.
23. P. G. De Gennes, J. Prost, *The Physics of Liquid Crystals* (Clarendon, Oxford, 1993).
24. R. H. Hurt, Z.-Y. Chen, *Phys. Today* **53**, 39 (2000).
25. This work was carried out at Synchrotron Stanford Synchrotron Radiation Laboratory, which is supported by the Division of Chemical Sciences of the Office of Basic Energy Sciences of the U.S. Department of Energy. We thank A. Cossy-Favre for help with some of the experiments.

14 February 2001; accepted 7 May 2001

Acoustic Oscillations in the Early Universe and Today

Christopher J. Miller,[1] Robert C. Nichol,[1] David J. Batuski[2]

During its first ≃100,000 years, the universe was a fully ionized plasma with a tight coupling by Thompson scattering between the photons and matter. The trade-off between gravitational collapse and photon pressure causes acoustic oscillations in this primordial fluid. These oscillations will leave predictable imprints in the spectra of the cosmic microwave background and the present-day matter-density distribution. Recently, the BOOMERANG and MAXIMA teams announced the detection of these acoustic oscillations in the cosmic microwave background (observed at redshift ≃ 1000). Here, we compare these CMB detections with the corresponding acoustic oscillations in the matter-density power spectrum (observed at redshift ≃ 0.1). These consistent results, from two different cosmological epochs, provide further support for our standard Hot Big Bang model of the universe.

The standard model of cosmology is the Inflationary Hot Big Bang scenario. A key aspect of this model is the ease with which it explains some critical observational facts about the universe. For example, the existence of the cosmic microwave background (CMB) radiation that fills all space is simply the radio remnant of a hot early phase of the universe, i.e., when it was only ≃100,000 years old. The model also provides a natural explanation for Hubble's famous expansion, large-scale coherent structures in the mass distribution (caused by quantum effects in the early universe), as well as producing a flat global geometry for the universe (*1*). In this scenario, the distribution of matter on the largest scales is connected, through well-established physics, to the temperature fluctuations in the CMB. Thus, any independent agreement between the CMB (at redshift ≃ 1000) and the matter-density distribution (at redshift ≃ 0.1) is naturally explained by the Hot Big Bang Inflationary model.

The early universe was a plasma made up of photons, electrons, and protons, along with the so-called Dark Matter. During this period, the gravitational force from potential wells (created as a result of local curvature pertubations or dark matter clumps) causes compressions in this fluid. As the plasma collapses inward, it meets resistance from photon pressure, reversing the plasma direction and causing a subsequent rarefaction. This cycle of compression and rarefaction results in acoustic oscillations, where baryons act as a source of inertia. Compression (rarefaction) of the plasma creates hot (cold) spots in the temperature of the plasma. Because the photons and baryons are coupled through Thompson scattering, the matter-density power spectrum will also exhibit these oscillations. As the universe cooled and the photons and matter decoupled, the acoustic oscillations became frozen as oscillatory features in both the temperature and matter-density power spectra. These acoustic oscillations are a general prediction from gravitational instability models of structure formation (*2*, *3*).

The recent results from the MAXIMA and BOOMERANG CMB balloon experiments provide evidence for the first two acoustic peaks (*4*–*8*). These acoustic oscillations are the peaks and valleys in Fig. 1A. The location and amplitude of the first peak indicate that

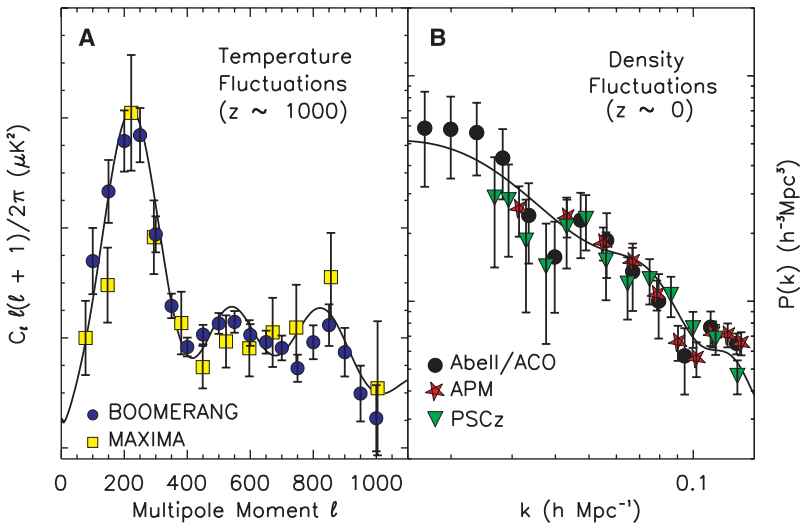

Fig. 1. We plot the CMB data from the MAXIMA and BOOMERANG experiments (**A**) alongside the matter-density data (**B**). The solid line is the best fit model (Ω_{matter} = 0.24, $\Omega_{baryons}$ = 0.06, and n_s = 1.08 with H_0 = 69) using the matter-density data alone. The amplitudes in both plots remain a free parameter. The solid line in (A) is not a fit to the CMB data (although the χ^2 is 34 for 32 data points). It is the resultant cosmological model using the best fit parameters from (B) and Ω_{vacuum} = 0.8, consistent with the Type Ia supernovae results (*18*).

[1]Department of Physics, Carnegie Mellon University, Pittsburgh, PA 15213, USA. [2]Department of Physics and Astronomy, University of Maine, Orono, ME 04469, USA.